Ultra-tough architected adhesive joints for integrated composite processing and bonding

Charline van Innis[1*], Michal K. Budzik[2], Thomas Pardoen[1,3]

[1]*Institute of Mechanics, Materials and Civil Engineering (iMMC), UCLouvain, Louvain-la-Neuve, Belgium (charline.vaninnis@uclouvain.be , thomas.pardoen@uclouvain.be)*

[2]*Department of Mechanical and Production Engineering (MPE), Aarhus University, Aarhus, Denmark (mibu@mpe.au.dk)*

[3]*Wel Research Institute, avenue Pasteur, 6, 1300 Wavre, Belgique*

**Corresponding author: charline.vaninnis@uclouvain.be*

ABSTRACT

Deployment of advanced polymer-based composites in critical structures requires, among others, breakthroughs in adhesive bonding solutions. Indeed, available methods suffer from limited fracture toughness of adhesives and from time-consuming bonding processes. Here, we demonstrate a novel concept of architected thermoplastic joints with exceptional fracture resistance larger than 5000 J/m² (4267 ± 846 J/m²), fully integrated with the composite resin transfer molding process, hence simultaneously targeting both limitations. This extreme toughness is activated through controlled 3D printed hollow pattern within a Nylon bondline. A synergetic combination of plastic dissipation, crack deflection, branching and arrest is tuned by changing the pattern characteristics. Three failure regimes are unraveled through fractographic analyses and finite element models. A stress-at-a-distance fracture criterion, identified for each constituent, quantitatively predicts the toughness variations along the crack path. This approach, amenable to dissimilar bonding between metals and composites, paves the road towards novel and higher performance structures and manufacturing approaches.

KEYWORDS*:* adhesive bonding, composites, fracture toughness, integrated manufacturing

1. Introduction

Carbon fiber reinforced polymer composites (CFRPs) are broadly used in advanced structures such as in airplanes, wind turbine blades or marine structures, owing to a high strength and stiffness to weight ratio. Manufacturing these structures often requires assembling CFRPs together or with other materials. Depending on the application, the adhesive thickness can vary from ~100 µm (e.g. aeronautic) to several centimeters (e.g. windmills or marine structures) [1]. Primary load carrying structures are frequently joined through mechanical fasteners, altering the composites structural integrity [2]. Adhesive bonding offers more uniform stress distribution and additional weight saving. However, limited resistance to crack propagation and long sequential bonding processes remain two barriers for more intensive use of this technology [2].

Adhesive bonding is a time and labor-intensive process involving careful surface treatment to reach acceptable mechanical performances [3]. Adherends join upon curing of the adhesive under clean and controlled environment. Co-curing is an attractive alternative enabling the simultaneous bonding and composite curing, without an adhesive, hence reducing the number of steps and removing the need for surface treatments. Integrated manufacturing of joints can be achieved through classical composite processes such as resin transfer molding (RTM), i.e. the interface between the two adherends can be seen as the bondline, made of a thin resin matrix layer. However, even high performance epoxy resins such as RTM6 [4,5] are significantly more brittle than the best adhesives, characterized by a fracture toughness typically lower by one order of magnitude. This sets a major challenge for the development of tough joints.

Several strategies have been proposed to enhance the crack propagation resistance of adhesive joints. Figure 1a shows a double cantilever beam (DCB) joint made of two composite adherends (gray), a “bondline” (blue) and two interlayers (yellow) corresponding to a thin surface layer of polymer matrix on the composite adherends. Many failure scenarios can be anticipated based on which class of toughening mechanism is activated. Enhanced plastic dissipation is the primary known mechanism to toughen adhesive joints [6]. Plastic dissipation (Figure 1-i) is dependent upon adhesive thickness [7–10]. In the presence of a soft layer (Figure 1-ii) adjacent to the layer where crack propagates, plastic dissipation can take place, enhancing the fracture toughness [11,12].

Crack deflection and zigzagging requires more energy than straight mode I cracks as a result of the introduction of a mode II component (Figure 1b-iii). Sinusoidal interfaces [13,14] and squared interfaces [15] have been designed to increase the crack surface area. Adding surface features [16,17] and modifying surface roughness [18,19] also improves mechanical interlocking. In homogeneous materials, crack deflection can also be triggered through stiff particles [20] or cavities [21] (Figure 1b-iv). The influence of the relative position of pores with respect to the crack leads to crack trapping and anti-shielding (i.e. an effective G_{Ic} lower than the local material G_{Ic}) if located ahead of the crack tip.

Crack trapping by cavities leads to crack tip blunting [22–24] (Figure 1b-v) with a positive effect on fracture toughness as the crack must reinitiate to further propagate. If the cavities are large with respect to the layer thickness and close to each other, the joint may behave as pillar interfaces [25] (Figure 1b-vi). More generally, metamaterials can be used as bondline to improve the fracture toughness [26].

Varying the local properties of the adherends or of the adhesive is one additional toughening strategy (Figure 1b-vii). Morano et al. [27] designed adherends with channels (Figure 1b-viii) to improve crack propagation resistance, involving parameter optimization. The adherend-adhesive interface strength through surface treatment can also be locally varied to force crack meandering from one weaker zone to another [28–30]. This further leads to bridging ligaments by alternating the strong interface zones [22,31]. Crack bridging proved to be a very efficient toughening mechanism. Thermoplastics veils [32,33] are, for these same reasons, inserted in composites to improve the interlaminar fracture toughness. Metallic [22] and polymeric [34] meshes in adhesive joints can be inserted to emulate this mechanism (Figure 1b-ix).

The first major challenge addressed in this study is to simultaneously activate most of the toughening principles to anticipate all possible failure scenarios and avoid a weak link option for crack propagation, and to reach joint toughness values unattainable with homogeneous joints. A key element to implement this vision is to consider the strength of the different interfaces which are: (i) the composite resin – carbon fibers interface for the interlayer-composite interface, (ii) the interface between the interlayer and the central bondline, i.e. between two polymers. For the latter, chemical interactions between compatible polymers can lead to tough interfaces [35]. Polyamide (PA), polyetherimide (PEI), polyethersulfone (PES), polycarbonate (PC) and polyetheretherketone (PEEK) are good candidates to promote a tough interface (Figure 1b-x). The second objective is to integrate the bonding step into a seamless manufacturing process. This implies insertion of the architected bondline at the midplane of the composite before resin injection. The architecture is designed to trigger most of the toughening mechanisms addressed above for all possible scenarios of crack propagation. To embody this vision, the core novelty has been the design of a bondline made of 3D printed Nylon (PA) thin bands with regularly spaced channels, which consists of a tough polymer but sufficiently soft (owing to the presence of cavities). The 3D printed film is shown in Figure 3a. Upon injection, two extreme joint configurations can be produced with either (i) all channels filled by resin or (ii) all left empty depending whether the channels are left open or not at the edges of the film. In addition, some intermediate configurations are obtained with (iii) the filling of only a fraction of the channels. In case (i), crack deflection is prevented, but local variation of properties can lead to crack trapping. Case (ii) can potentially lead to the behavior observed for pillar interfaces when the crack propagates in the central layer [25]. Case (iii) permits a combination of the two modes. As the mechanical resistance under shear loading is also important in applications, it will be addressed by finite element modelling to determine the influence of architecture. Eventually, the Ashby's material selection approach [36] is used to analyze the trade-off between toughness and shear resistance.

2. Materials and methods

2.1. Joints manufacturing

Figure 2 schematically outlines the bonding process from the architected film printing to final joint (see Supplementary Material for a description of the full process). The Nylon structures, layer height of 100 µm, are 3D printed using NylonWhite material (supplied by Markforged) on a MarkTwo machine with the default/optimized manufacturer settings. The design rules for adherends with channels set by Morano et al. [27] based on finite element simulations are used to select the height (*H*), the width (*W*) and the spacing (*S*) between the cavities. The total bondline thickness is referred as *t*. These authors found that G_{Ic} is maximized if *H/t* has the largest possible value (0.65 in their study), if *W/H* is equal to 1.25 and if *S* is equal to *W*. In addition to these rules, the structure thickness is set by the available RTM mold. The dimensions are: thickness of 1.4 mm, cavity height and width of, respectively, 1 mm and 1.2 mm and spacing between cavities is equal to 1 mm. The 3D printed structure, shown in Figure 3a, is inserted at the midplane of the composite in the mold after visual inspection. The two composite adherends are made of four plies of H5 satin fabric made of carbon fibers each (HexForce G0926 supplied by Hexcel). At the midplane, in addition to the architected Nylon tape, a non-adhesive polyimide (Kapton) film is inserted to create a pre-crack required for DCB fracture testing. Once the RTM mold is closed by a pressure of 8 bars, the epoxy resin RTM6 from Hexcel is injected at a temperature of 90°C. Then, the temperature is increased up to 160°C at a rate of 2°C/min and this temperature is held for 90 minutes before increasing it up to 180°C at the same rate, with a post-curing duration of two hours. During injection, the pressure inside the mold is increased and maintained to 6 bars. Upon curing, the channels have a height of 0.8 mm and a length of 1.1 mm, with 1 mm spacing (Figure 3d).

2.2. Mechanical testing

The DCB samples, shown in Figure 3a, have been machined from the cured panels with a length of 200 mm and a width of 20 mm. The 70 mm long Kapton film inserted to create the precrack results in initial crack length of 50 mm. The total height of the samples is about 4.4 mm including the structured insert of 1 mm. The DCB tests are performed following the ISO 25217 standard on a Zwick/Roell machine equipped with a 50 kN loadcell, at constant cross-head speed of 1 mm/min. The crack tip position is tracked using Digital Image Correlation (DIC) using two cameras and the Istra4D software. For the DIC analysis, the facet size and the grid spacing are set to 21 and 7 pixels, respectively. G_{Ic} is then computed following the single beam theory. As large deflections take place, the corrected beam theory and the experimental compliance method should be preferred but cannot be applied in the present case due to the stick-slip behavior [37] which introduces some uncertainty on the exact value of G_{Ic}.

Tensile tests are performed, using the same mechanical testing machine and settings as before, on flat dogbone NylonWhite specimens to determine the tensile properties. The specimens shown in Figure 3b have a thickness of 2 mm and width of 5 mm along the 30 mm long gauge section. Extensometers with an initial spacing of 20 mm are used to determine the strain.

2.3. Fractography

For fractography analyses, scanning electron microscope (SEM) and optical microscope have been used. An Ultra 55 Field-Emission SEM (Zeiss, Germany) has been used to analyze the fracture surfaces with a voltage of 5 keV. An Olympus Provis AX70 optical microscope has been used to analyze fractured joints. This required to cut the joints along the crack propagation direction and to polish the cross-section prior to observation.

3. Finite element modelling

Two finite element (FE) models are developed. The first one is for the DCB configuration and is used to investigate the failure mechanisms taking place in the architected joints and observed experimentally. The second one addresses the lap-shear joint configuration to investigate the influence of the architected film and of the position and fraction of filled /empty cavities in the joint on the shear properties.

3.1. Double Cantilever Beam configuration

The DCB specimen with 100 mm length, 50 mm pre-crack and 20 mm width is modelled using the commercial FE code Abaqus (Dassault Systemes, France). A 2D model is created with four-nodes plane-strain elements with reduced integration (CPE4R) to perform computations under static conditions. Different configurations are modelled by varying the channels left empty or filled by resin to determine how the fracture toughness is affected when varying some key parameters based on a failure criterion of the type "maximum principal stress at a critical distance". Six cavities are considered, but only the state of the third, fourth and fifth cavities in Figure 4a is changed. If a joint made of only empty cavities is modeled, 12 channels are considered in the model. The initial crack is introduced as a seam and the mesh is refined around the crack tip with the smallest elements having a length of 5 μm. Different meshes have been tested to check the convergence of the results in terms of mesh refinement.

Regarding the material properties, the Nylon tensile test data of Figure 4c and data from previous experimental campaigns of our laboratory are used for the epoxy resin and the composite (Figure 4c-d). The composite is characterized by an in-plane Young's modulus of 70 GPa, an out-of-plane modulus equal to 3 GPa and a Poisson ratio equal to 0.3 [5]. The epoxy resin behavior is modelled with isotropic linear elasticity and with the Drucker-Prager yield criterion for the plastic response, see Morelle et al. [38].

The failure criterion requires the determination of a critical stress associated to a critical distance for each material and interface. Such a two-parameter criterion has been shown to better capture thickness effects than cohesive zone models in adhesive joints [39]. The crack is assumed to propagate in the channels filled by RTM6 resin when the maximum principal stress is equal to 300 MPa over a distance of 10 μm, as identified in a former study [4]. Although the tensile strength of the Nylon is equal to 136 MPa (when tested in the longitudinal direction, see Figure 4c), a value of 50 MPa is used for the critical stress in this case. This low value is justified by the significant anisotropy in the fracture resistance associated to the 3D printing process which potentially leads to much smaller cracking resistance in the direction orthogonal to the printed layers. Furthermore, a larger critical stress leads to extreme deformation close to the crack tip and to convergence issues before fulfilling the criterion. Hence, the choice of the 50MPa value at a distance of 200 µm for the printed Nylon is much more phenomenological (and based on extrapolating data from Kinloch and Williams [40]) than the values chosen for RTM6 which were based on a systematic analysis of the fracture mechanisms [4]. The interface with the composite is assumed to fail when the maximum principal stress is equal to 50 MPa over a distance of 100 µm. When one of the failure criteria is met, the corresponding applied load P is extracted in order to determine G_{Ic} using the ISO 25217 standard:

$$G_{Ic} = \frac{4P^2}{EW^2}\left(\frac{3a^2}{h^3} + \frac{1}{h}\right), \quad (1)$$

and the orientation of the maximum principal stress is also extracted in order to determine the crack propagation direction.

3.2. Single lap shear joint configuration

A lap joint shown in Figure 4b made of the architected film comprising six cavities that can be either filled or left empty is modelled. The adherends length, width and height are set to 100 mm, 20 mm and 1.7 mm, respectively. The channels are symmetrically distributed. A 10 µm thick resin layer is modelled between the composite adherends and the architected film. As for the DCB simulations, CPE4R elements are used as well as the same material constitutive laws as described earlier. In addition, the fraction and position of the filled cavities are varied. The shear strength is computed when one of the failure criteria described above is met.

4. Results and discussion

4.1. Mode I fracture toughness

The experimental crack resistance curves are given in Figure 5a while Figure 5b shows a typical crack resistance curve giving the variation of mode I critical energy release rate, G_{Ic}, as a function of crack growth Δa (see Supplementary Information S1 for all results). Three regimes of G_{Ic} are distinguished. The configurations associated to these regimes is shown in Figure 5c, as well as the G_{Ic} values predicted by the FE model. Regime (1) is characterized by G_{Ic} between 600 and 1200 J/m² (precisely 828 ± 157 J/m²). Regime (2) corresponds to 1500 to 2500 J/m² (precisely 1704 ± 422 J/m²) while the largest G_{Ic} are above 3000 J/m² (precisely 4267 ± 846 J/m²) up to exceptionally high values larger than 5000 J/m² in regime (3). For comparison, the interlaminar toughness of composite made of G0926 carbon fibers fabrics and RTM6 is ~350 J/m². Adhesives used in aerospace such as FM300 or EA9695K05 have G_{Ic} in the range 800 to 1000 J/m² [41]. The two best regimes exhibit a resistance 1.5 to 5.5 times of classical adhesives while being produced in a single co-curing step. Even the lowest Regime (1) results in resistances higher than the interlaminar toughness. Independent or not of the presence of a weaker regime, ultimately, crucial for crack propagation resistance is the presence of a strong crack arrestor mechanism as triggered in the present joints.

In Regime (1), Figure 6a-b shows that the crack propagates along the interface between the composite and Nylon structure. The variations originate from the coexistence of three sub-mechanisms. First, broken fiber bundles along the Nylon side indicate that fiber bridging is activated (Figure 6b) with, we assume, only a minor toughening role - the H5 satin fabrics are indeed known for involving limited contribution of fiber bridging to G_{Ic} [42,43]. Subsequently, the crack propagates between two adjacent 3D printed layers resulting in small bridging ligaments. The crack deflection between two printed layers has not been fully elucidated, but probably originates from poor local adhesion between layers. Finally, the main path is along the composite-Nylon interface where the crack is not deflected into the composite or into the Nylon structure. Opposite to the current results, Tao et al. [31] inserted a PA film in the middle of an adhesive layer, but with a detrimental effect on G_{Ic}. This configuration including only filled cavities is modelled by finite elements. As shown in Figure 6c, the computed G_{Ic} varies from 490 to 1550 J/m² depending on the crack tip location. This comes from the difference in energy dissipated by plastic deformation. Indeed, when the crack is located above a filled channel, the plastic zone is constrained by the stronger epoxy resin in the channel. An increase in fracture toughness above the channels due to the higher local stiffness as in Morano et al. [27] was expected opposite to the present results. This indicates a competition between the contribution of plastic dissipation and the effect of stiffness variations. In the present case, plastic dissipation dominates. In addition, when the crack tip is located between two adjacent cavities, stresses first concentrate at the interface above the filled channel ahead of the crack tip, leading to the initiation of a secondary crack that interacts then with the main crack. Plastic dissipation in the Nylon film thus contributes to the toughness associated to Regime (1) as it acts as a dissipative layer [11,12]. In addition, 3D printing generates some roughness on the film surface that can lead to mechanical interlocking also contributing to the increase in fracture toughness.

The second regime corresponds to crack trapping by a channel (Figures 5b and 7) left empty upon resin injection, while the others are filled as shown in Figure 7a-b. The finite element model shows that when the crack is located at the interface above the last filled channel before the void, stresses tend to concentrate between the crack tip and the cavity, see Figure 7c. This leads to crack deflection towards the cavity when the failure criterion is met, and it becomes trapped by the empty channel. Although the crack propagates through Nylon, the Nylon fracture toughness is not attained as the void leads to an anti-shielding effect [44] resulting in the apparent fracture toughness equal to about 1500 J/m² in the simulation. The micrographs show that the crack propagates through the tough Nylon film from the cavity towards the same interface as previously. In this case, the finite element model indicates, as observed in Figure 7d, that stress concentrates at the interface close to the filled channel ahead of the void resulting into the initiation of a small crack that progressively propagates. At some point, the secondary crack and the main crack interact and join each other, see Figure 7e, leading to the main crack propagation. This mechanism is summarized in Figure 7f and the computed fracture toughness is about 2500 J/m². In addition, the main crack is not sharp and, as explained by Maloney and Fleck [22] and Heide-Jørgensen et al. [23,24], the crack tip gets extensively blunted and must then re-initiate, improving the joint toughness. Propagation of the crack through the tough Nylon contributes to the G_{Ic} improvement, although the bulk G_{Ic} of Nylon is never attained. The experimental scatter on G_{Ic} is explained by the partial filling of some of the channels (Figure 7b). Deflection is observed when the channel is empty at least over one third of the joint width. In this case, only a small part of the crack front is trapped by the empty cavity while the rest of the crack still propagates along the weak composite-Nylon interface. To conclude, the toughness of Regime (2) is due to the crack propagation inside the tough Nylon film originating from its deflection by the channel and its deflection back to the interface when reinitiated due to the initiation of microcracks along the interface.

Regime 3, observed in Figure 8, is triggered when the crack propagates through the thickness of the film, from one interface to the other. This crack path is observed for all the points, obtained on different specimens, characterized by a fracture toughness larger than 3 kJ/m² in Figure 5a. The fractography could not reveal the root cause of this deflection. Although the crack is arrested for the cases for which the crack is trapped by an empty channel or when it propagates through the entire thickness of the structure, an unstable crack propagation jump is observed along the weak composite-Nylon interface when reaching G_{Ic}. It is deemed that it originates from a sudden change in the adherence at one of the interfaces. The top interface in Figure 8c is stronger than the bottom one, leading to the crack deflection at the weakest interface (Figure 8c-e) as it has been reported by Tao and co-workers [45]. This is modeled by inserting a secondary crack at the bottom interface. It can be observed in Figure 8f-g that the two cracks interact with each other and that the primary crack propagates through the Nylon film. A maximum fracture toughness of about 4300 J/m² is computed using the FE model for this Regime 3, in very good agreement with the experimental results.

In addition to these three experimental observations, FE simulations have been performed for other configurations in order to guide towards even larger theoretical joint design. First, a joint made only of empty channels is modelled. In this case G_{Ic} reaches 40 kJ/m² with the Nylon structure acting as bridging ligaments. This value is extremely high and, although most probably unrealistically high, but provides a motivation for further optimization. However, when one wall fails, a large amount of energy is released which is not considered by the model and could be detrimental to structural integrity. However, under the displacement-controlled conditions, when one of the walls fails, the energy will be released following unloading paths. Thus, once the next wall is attained, the energy stored in the loaded composite beams will be much lower than the fracture energy and the propagation is altered [24] . In addition, integrated manufacturing of such joint is complicated, asking for perfect control of the printing process preventing the resin from entering the channels. Note that other failure scenarios could take place such as composite delamination and, though not considered by the model.

As a further step, the influence of the second channel ahead of the cavity on the failure process has been considered (Appendix 1). The process zone length is evaluated (Figure A.1a) to be around 3 to 4 mm. Given the channels dimension, the second cavity ahead of the crack tip could also have an influence on G_{Ic}. An empty channel has a shielding effect (Figure A.1b-e), leading to higher G_{Ic}. Thus, an empty channel can result in two antagonistic effects depending on its position with respect to the crack tip, i.e. anti-shielding if located ahead and shielding if located far enough.

4.2. Lap shear joints

The fracture toughness of the joint is not the only important property to consider when designing bonded joints under shear dominated loads. In aerostructures, the adhesive thickness must remain below a certain threshold to limit the decrease of shear stiffness and strength. This has been addressed, using as an example, the lap shear joint configuration with the architected bondline. For this purpose, the number of empty and filled channels varies as well as the position. Table 1 shows that increasing the number of filled cavities improves the joint strength and stiffness. However, it can also be observed that, for a given amount of filled channels, the position of the filled channels does influence the shear strength.

First, the two extreme cases, EEE and FFF models, are compared to one another. Figure 9a-d shows that, for a given applied load, shear stresses are smaller in the joint with all channels being filled. This arises from the fact that by filling the channels, the effective cross-section area over which the applied shear force act is increased, reducing the magnitude of the local shear stresses. In addition, filling all the cavities also results in lower peel stresses near the edges. Regarding the failure locus, the criterion is first met at the joint corner for EEE while it is first met in the interface above the first filled cavity for FFF. The shear strength is thus improved by increasing the amount of filled channels, but also the shear stiffness, as when filling all the cavities, a stiffer material is present in the bondline.

When joints containing 33% and 66% of filled channels are considered, an influence of the location of the empty and filled channels with respect to the joint edges is found (Table 1). Indeed, if the channel close to the edge is left empty, the shear strength is improved with respect to the case for which the edge channels are filled with resin. The stress distributions are shown in Figure 9e-h for the FEE and EEF joints, both containing 33% of filled channels. The shear stresses (Figure 9e, g), in both situations, are the highest right above the filled cavity. Regarding the peel stresses, they tend to be the highest near the joint edges in both cases, but their magnitude is slightly larger when the first channel is left empty which could negatively affect the shear strength. However, due to the combination of the large peel stresses and the shear stresses near the filled channel when located near the edge, the failure criterion is first met for the joint with the filled channel near the edges, resulting in a lower shear strength. The introduction of an empty channel near the joint edges thus improves the stress distribution and the shear strength. The same accounts for a joint containing 66% of filled channels.

These findings agree with common results found in the literature. Indeed, Kumar et al. [46] tailored the stiffness of adhesive bonds. They determined an improved strength when the center of the joint is stiffer than the edges. Here, a larger shear strength has been found when for a given amount of filled cavities, the empty cavities are located at middle of the joint. When the edge activity is left empty, peel stresses near the joint corners tend to be larger. However, shear stresses near the edge are lower and the cavity allows for better shear stress distribution in the joint, resulting in higher shear strength. Indeed, when the first channel is filled, high shear stresses localize near the corner, in the interface right above the filled cavity leading to premature failure.

As a further perspective, it would be interesting to investigate the influence of the amount of filled channels and their position in the joint for industrial assembly by using a more complex model.

5. Materials selection for joints with tunable properties

In the previous section, the influence of the position of the filled and empty channels on the joint properties have been investigated. Contrary to the fracture toughness, stiffness and strength are improved by increasing the amount of filled channels (Table 1). Hence, depending on the joint configuration, the properties of the joint can be modified. To determine the best joint configuration, a rational materials selection procedure [36] has been followed as further developed elsewhere [47]. The objective of the selection chosen here is to minimize the mass of the structure, $m = \rho LWt$ with ρ the density of the architected film, L and W the length and width of the joint, and *t* the film thickness. The joint is subjected to two forces: a tensile force F_σ and a shear force F_τ (Figure 10a) resulting in a tensile stress $\sigma_\perp$ and a shear stress τ. This leads to two constraints: (1) F_σ cannot lead to crack propagation in the presence of a crack of length $2a$ implying that $K < K_{IC}$ and (2) F_τ cannot result in a displacement larger than $u_\tau|_{max}$. Through FE modelling, the joint stiffness and fracture toughness are computed for different amount of filled cavities (0, 33, 66, 100 %) and architected film thicknesses ranging from 0.05 to 1 mm. It is important to recognize that small film thicknesses cannot be used with the current manufacturing procedure but could be produced with other techniques such as selective laser sintering, stereolithography or selective thermoplastic electrographic process. The lowest attainable film thickness is thus a matter of access and progress in 3D printing technology. If the joint is mainly subjected to tensile stresses (Figure 10b), the selection is dominated by G_{Ic} and the best joint is made of empty cavities. On the other hand, if only shear is applied to the joint, the shear stiffness constraint dominates (Figure 10c), the best joint contains 66% or 100% of filled cavities. These two examples show that depending on the loading, the best configuration changes. The degree of freedom in the architecture allows tuning performances depending on the application to get an optimum response. Further work will focus on extending this selection analysis to a wider range of objectives, constraints and load configurations as attempted elsewhere for mainly classical adhesives [47].

6. Conclusion

Intensive use of adhesive bonding in composite applications is prevented by the moderate fracture toughness of available adhesives and long manufacturing times. To simultaneously unlock these two barriers, we printed architected Nylon films with channel holes to bond composites by co-curing. This leads to several major findings:

- First, exceptionally high fracture toughness larger than 5000 J/m² is attained during crack propagation with intermediate regimes also of high fracture toughness. Several toughening mechanisms are triggered involving: plastic dissipation, crack deflection, crack tip blunting and crack shielding.
- Second, single step co-curing is enforced by simultaneously bonding and processing of the composite panels, saving time and energy, and avoiding surface treatments.
- Third, the shear stiffness and strength can be modulated by playing with the architecture depending on the structural requirements.
- Aside from proving excellent toughening potential, this study made use of the simple stress-at-a distance failure criterion. This failure criterion proved very effective to predict the magnitude of G_{Ic} for the different cracking mechanisms occurring along the crack path after identification from independent data on the bulk materials under consideration.
- An original materials selection approach is adapted to adhesive joints to guide the design approach of the best joint configuration depending on the application.

As a perspective, controlling the filling of the cavities and the film thickness can lead to a wide variety of ultra-tough joints with controlled strength and stiffness based on a single architected film. However, controlling the film thickness requires to change of manufacturing technique which is left for further investigation.

Appendix 1: Influence of the second cavity ahead of the crack tip

An important parameter to consider when designing architected joints is the length of the process zone. Heide-Jørgensen and Budzik [24] define it as the inverse of the elastic foundation wavelength λ for adhesive joints given by

$$\lambda = \sqrt[4]{\frac{m}{4}\frac{E_a}{t_a}\frac{W}{EI}}, \qquad (A1.1)$$

where E_a and t_a are, respectively, the Young's modulus and the thickness of the adhesive which has a Poisson ratio ν_a, the composite modulus *E*, the DCB width *W*, the second inertia moment *I* while *m* defines the stress state at the crack tip in the following way:

- For plane-strain conditions and plane stress conditions in the transverse direction: $m = 1/(1-\nu_a^2)$;
- For plane strain conditions in in-plane and out-of-plane directions: $m = (1-\nu_a)/[(1-2\nu_a)(1+\nu_a)]$;
- For plane stress conditions in all directions: $m = 1$.

Assuming that the central layer is made of NylonWhite only, this equation leads to values of process zone lengths ranging from 3.12 mm to 3.95 mm. As the length of one channel is 1.1 mm and the spacing between two adjacent channels is 1 mm, when the crack is located above the right (crack A) or the left (crack B) corner of a cavity, the process zone spans over cavity III as shown in Figure A.1a. Consequently, channel III must be considered.

Leaving cavity III in Figure A.1a empty has a beneficial effect as the computed fracture toughness corresponding to when the first failure criterion is met is higher. Depending on the case, the fracture toughness is increased by 10 to 25% when the cavity III is left empty. When the two first cavities (I and II) are filled and if cavity III is empty, the fracture toughness is improved by 7 to 15% when the crack propagates along the composite interface between the two first channels. The improvement is only 7% when it is close to the right corner of cavity I while the increase is of 15% when the crack is close to cavity II. The stress distributions in this last case are shown in Figure A.1b-c for an arbitrary load applied on the DCB. The stresses near the crack tip are lower when the last cavity is left empty. If channel I is empty while channel II is filled, the fracture toughness increases by 25% if cavity III remains empty. The maximum principal stress distributions are shown in Figure A.1d-e, with lower stresses near the interface when cavity III is empty. To conclude, if the empty cavity is located far enough from the crack tip and is located in the process zone, it has a shielding effect while it has an anti-shielding effect when it is close from the crack tip (this is the case where the crack is deflected towards the cavity).

Acknowledgments

C.vI. is a FRIA grantee of the Fonds de la Recherche Scientifique de Belgique - FNRS and gratefully acknowledges their support. The authors gratefully acknowledge Dimitri Gueuning, Nicolas Van Hille and Thibaut de Lumeley Woodyear from Sonaca for the discussions and the supply of the carbon fibers and the RTM6 resin.

Author contributions

Charline van Innis: Conceptualization, Methodology, Software, Visualization, Formal analysis, Writing – original draft, Writing – review & editing

Michal K. Budzik: Writing – original draft, Writing – review & editing, Supervision

Thomas Pardoen: Conceptualization, Writing – original draft, Writing – review & editing, Supervision

Data availability

The data that support the findings of this study are available on request from the corresponding author C.vI.

Competing interests

A patent concerning this work has been submitted. The patent inventors are C.vI. And T.P. and the applicant institution is Université catholique de Louvain. The patent application has as title “Film for joining parts” and the patent application number is EP23161330.8. This patent application is pending. The remaining author, M.K.B., declares that he has no other competing interests.

References

[1] Budzik MK, Wolfahrt M, Reis P, Kozłowski M, Sena-Cruz J, Papadakis L, et al. Testing mechanical performance of adhesively bonded composite joints in engineering applications: an overview. J Adhes 2022;98:2133–209. https://doi.org/10.1080/00218464.2021.1953479.

[2] Pocius A V. Adhesion and Adhesives Technology. Third Edit. Carl Hanser Verlag GmbH & Co. KG; 2012. https://doi.org/10.3139/9783446431775.fm.

[3] Tao R, Alfano M, Lubineau G. In situ analysis of interfacial damage in adhesively bonded composite joints subjected to various surface pretreatments. Compos Part A Appl Sci Manuf 2019;116:216–23. https://doi.org/10.1016/j.compositesa.2018.10.033.

[4] Chevalier J, Morelle XP, Camanho PP, Lani F, Pardoen T. On a unique fracture micromechanism for highly cross-linked epoxy resins. J Mech Phys Solids 2019;122:502–19. https://doi.org/10.1016/j.jmps.2018.09.028.

[5] Hexcel. HexFlow ® RTM6, Product Data Sheet. 2018.

[6] Hutchinson JW, Tvergaard V. The relation between crack growth resistance and fracture process parameters elastic-plastic solids. J Mech Phys Solids 1992;40:1377–97.

[7] Bascom WD, Cottington RL, Jones RL, Peyser P. The fracture of epoxy- and elastomer-modified epoxy polymers in bulk and as adhesives. J Appl Polym Sci 1975;19:2545–62. https://doi.org/10.1002/app.1975.070190917.

[8] Kinloch AJ, Shaw SJ. The Fracture Resistance of a Toughened Epoxy Adhesive. J Adhes 1981;12:59–77. https://doi.org/https://doi.org/10.1080/00218468108071189.

[9] Pardoen T, Ferracin T, Landis CM, Delannay F. Constraint effects in adhesive joint fracture. J Mech Phys Solids 2005;53:1951–83. https://doi.org/10.1016/j.jmps.2005.04.009.

[10] Martiny P, Lani F, Kinloch AJ, Pardoen T. A multiscale parametric study of mode i fracture in metal-to-metal low-toughness adhesive joints. Int J Fract 2012;173:105–33. https://doi.org/10.1007/s10704-011-9667-x.

[11] Bertholet Y, Olbrechts B, Lejeune B, Raskin JP, Pardoen T. Molecular bonding aided by dissipative inter-layers. Acta Mater 2007;55:473–9. https://doi.org/10.1016/j.actamat.2006.08.036.

[12] Dépinoy S, Strepenne F, Massart TJ, Godet S, Pardoen T. Interface toughening in multilayered systems through compliant dissipative interlayers. J Mech Phys Solids 2019;130:1–20. https://doi.org/10.1016/j.jmps.2019.05.013.

[13] Cordisco FA, Zavattieri PD, Hector LG, Carlson BE. Mode I fracture along adhesively bonded sinusoidal interfaces. Int J Solids Struct 2016;83:45–64. https://doi.org/10.1016/j.ijsolstr.2015.12.028.

[14] Zavattieri PD, Hector LG, Bower AF. Determination of the effective mode-I toughness of a sinusoidal interface between two elastic solids. Int J Fract 2007;145:167–80. https://doi.org/10.1007/s10704-007-9109-y.

[15] Maloney K, Fleck N. Damage tolerance of an architected adhesive joint. Int J Solids

Struct 2018;132–133:9–19. https://doi.org/10.1016/j.ijsolstr.2017.06.010.
[16] Sun C, Thouless MD, Waas AM, Schroeder JA, Zavattieri PD. Ductile-brittle transitions in the fracture of plastically-deforming, adhesively-bonded structures. Part I: Experimental studies. Int J Solids Struct 2008;45:3059–73. https://doi.org/10.1016/j.ijsolstr.2008.01.011.
[17] Pascuzzo A, Yudhanto A, Alfano M, Lubineau G. On the effect of interfacial patterns on energy dissipation in plastically deforming adhesive bonded ductile sheets. Int J Solids Struct 2020;198:31–40. https://doi.org/10.1016/j.ijsolstr.2020.04.001.
[18] Shahid M, Hashim SA. Effect of surface roughness on the strength of cleavage joints. Int J Adhes Adhes 2002;22:235–44. https://doi.org/10.1016/S0143-7496(01)00059-8.
[19] Kim WS, Yun IH, Lee JJ, Jung HT. Evaluation of mechanical interlock effect on adhesion strength of polymermetal interfaces using micro-patterned surface topography. Int J Adhes Adhes 2010;30:408–17. https://doi.org/10.1016/j.ijadhadh.2010.05.004.
[20] Wang C, Libardi W, Baldo JB. Analysis of crack extension paths and toughening in a two phase brittle particulate composite by the boundary element method. Int J Fract 1998;94:177–88. https://doi.org/10.1023/A:1007591216796.
[21] Gockowski LF, Dolinski ND, Chavez R, Cohen N, Eisenreich F, Hecht S, et al. Engineering crack tortuosity in printed polymer-polymer composites through ordered pores. Mater Horizons 2020;7:1854–60. https://doi.org/10.1039/d0mh00331j.
[22] Maloney K, Fleck N. Toughening strategies in adhesive joints. Int J Solids Struct 2019;158:66–75. https://doi.org/10.1016/j.ijsolstr.2018.08.028.
[23] Heide-Jørgensen S, Budzik MK. Crack growth along heterogeneous interface during the DCB experiment. Int J Solids Struct 2017;120:278–91. https://doi.org/10.1016/j.ijsolstr.2017.05.013.
[24] Heide-Jørgensen S, Budzik MK. Effects of bondline discontinuity during growth of interface cracks including stability and kinetic considerations. J Mech Phys Solids 2018;117:1–21. https://doi.org/10.1016/j.jmps.2018.04.002.
[25] Heide-Jørgensen S, Budzik MK, Turner KT. Mechanics and fracture of structured pillar interfaces. J Mech Phys Solids 2020;137:103825. https://doi.org/10.1016/j.jmps.2019.103825.
[26] Athanasiadis AEF, Dias MA, Budzik MK. Can confined mechanical metamaterials replace adhesives? Extrem Mech Lett 2021;48:101411. https://doi.org/10.1016/j.eml.2021.101411.
[27] Morano C, Zavattieri P, Alfano M. Tuning energy dissipation in damage tolerant bio-inspired interfaces. J Mech Phys Solids 2020;141:103965. https://doi.org/10.1016/j.jmps.2020.103965.
[28] Kendall K, A PRSL. Control of cracks by interfaces in composites. Proc R Soc London A Math Phys Sci 1975;341:409–28. https://doi.org/10.1098/rspa.1975.0001.
[29] Xu Y, Singh Y, Pan C, Subbarayan G. Adhesive toughness and instability in bonded heterogeneous films. Int J Solids Struct 2019;169:41–54. https://doi.org/10.1016/j.ijsolstr.2019.04.003.
[30] Budzik MK, Jumel J, Shanahan MER. Impact of interface heterogeneity on joint fracture. J Adhes 2012;88:885–902. https://doi.org/10.1080/00218464.2012.725604.
[31] Tao R, Li X, Yudhanto A, Alfano M, Lubineau G. Toughening adhesive joints through crack path engineering using integrated polyamide wires. Compos Part A Appl Sci Manuf 2022;158:106954. https://doi.org/10.1016/j.compositesa.2022.106954.
[32] Kuwata M, Hogg PJ. Interlaminar toughness of interleaved CFRP using non-woven veils: Part 1. Mode-I testing. Compos Part A Appl Sci Manuf 2011;42:1551–9. https://doi.org/10.1016/j.compositesa.2011.07.016.
[33] Quan D, Flynn S, Artuso M, Murphy N, Rouge C, Ivanković A. Interlaminar fracture toughness of CFRPs interleaved with stainless steel fibres. Compos Struct 2019;210:49–56. https://doi.org/10.1016/j.compstruct.2018.11.016.
[34] Yudhanto A, Almulhim M, Kamal F, Tao R, Fatta L, Alfano M, et al. Enhancement of

fracture toughness in secondary bonded CFRP using hybrid thermoplastic/thermoset bondline architecture. Compos Sci Technol 2020;199:108346. https://doi.org/10.1016/j.compscitech.2020.108346.
[35] Deng S, Djukic L, Paton R, Ye L. Thermoplastic-epoxy interactions and their potential applications in joining composite structures - A review. Compos Part A Appl Sci Manuf 2015;68:121–32. https://doi.org/10.1016/j.compositesa.2014.09.027.
[36] Ashby MF. Materials Selection in Mechanical Design. 5th ed. Oxford: Butterworth-Heinemann; 2017. https://doi.org/10.1016/b978-1-85617-663-7.00026-6.
[37] ISO. ISO25217 Adhesives — Determination of the mode 1 adhesive fracture energy of structural adhesive joints using double cantilever beam and tapered double cantilever beam specimens. 2014.
[38] Morelle XP, Chevalier J, Bailly C, Pardoen T, Lani F. Mechanical characterization and modeling of the deformation and failure of the highly crosslinked RTM6 epoxy resin. Mech Time-Dependent Mater 2017;21:419–54. https://doi.org/10.1007/s11043-016-9336-6.
[39] Martiny P, Lani F, Kinloch AJ, Pardoen T. A maximum stress at a distance criterion for the prediction of crack propagation in adhesively-bonded joints. Eng Fract Mech 2013;97:105–35. https://doi.org/https://doi.org/10.1016/j.engfracmech.2012.10.025.
[40] Kinloch AJ, Williams JG. Crack blunting mechanisms in polymers. J Mater Sci 1980;15:987–96. https://doi.org/10.1007/BF00552112.
[41] Mohan J, Ivanković A, Murphy N. Mode i fracture toughness of co-cured and secondary bonded composite joints. Int J Adhes Adhes 2014;51:13–22. https://doi.org/10.1016/j.ijadhadh.2014.02.008.
[42] Alif N, Carlsson LA, Boogh L. The effect of weave pattern and crack propagation direction on mode I delamination resistance of woven glass and carbon composites. Compos Part B Eng 1998;29:603–11. https://doi.org/10.1016/S1359-8368(98)00014-6.
[43] Kim JK, Sham ML. Impact and delamination failure of woven-fabric composites. Compos Sci Technol 2000;60:745–61. https://doi.org/10.1016/S0266-3538(99)00166-9.
[44] Rezanezhad M, Lajevardi SA, Karimpouli S. Effects of pore-crack relative location on crack propagation in porous media using XFEM method. Theor Appl Fract Mech 2019;103:102241. https://doi.org/10.1016/j.tafmec.2019.102241.
[45] Tao R, Li X, Yudhanto A, Alfano M, Lubineau G. On controlling interfacial heterogeneity to trigger bridging in secondary bonded composite joints: An efficient strategy to introduce crack-arrest features. Compos Sci Technol 2020;188:107964. https://doi.org/10.1016/j.compscitech.2019.107964.
[46] Kumar S, Wardle BL, Arif MF. Strength and performance enhancement of bonded joints by spatial tailoring of adhesive compliance via 3D printing. ACS Appl Mater Interfaces 2017;9:884–91. https://doi.org/10.1021/acsami.6b13038.
[47] van Innis C, Pardoen T. Thickness-dependent selection of adhesive joints. Submitt to J Adhes 2023.
[48] Granta. Granta EduPack 2021 R2 2021.

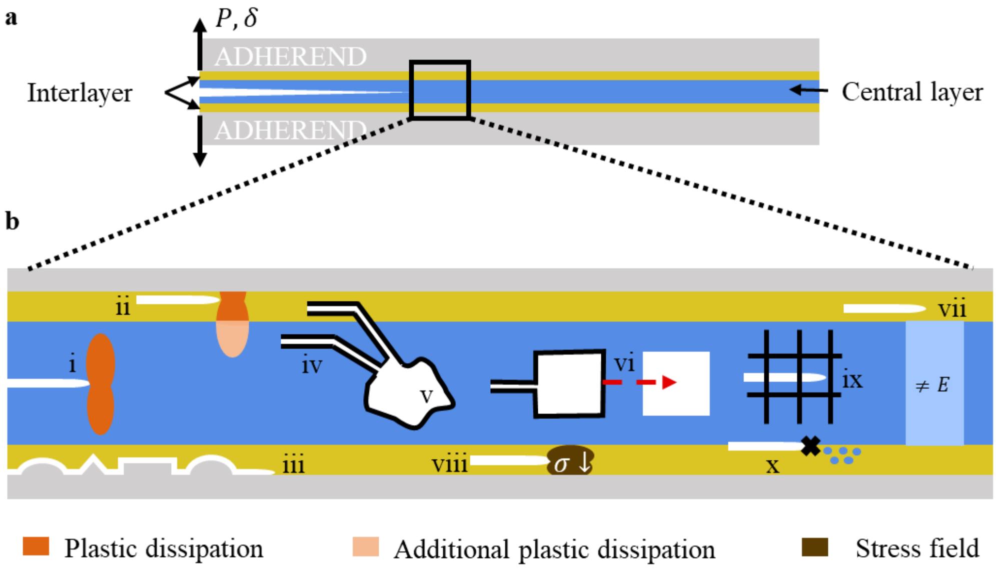

Figure 1: Schematic illustration of (a) a DCB joint with the composite adherends (gray), central bondline (blue) and two interlayers (yellow) on both sides, and (b) of the toughening mechanisms that can take place in the joint depending on the cracking mechanism – failure scenario. (i) Plastic dissipation, (ii) additional plastic dissipation due to soft layer, (iii) structured interface, (iv) crack deflection by cavity and (v) subsequent trapping and blunting, (vi) pillar interfaces, (vii) local stiffness variation, (viii) shielding by a cavity, (ix) crack bridging by a mesh and (x) tough interface due to polymer chemical interactions.

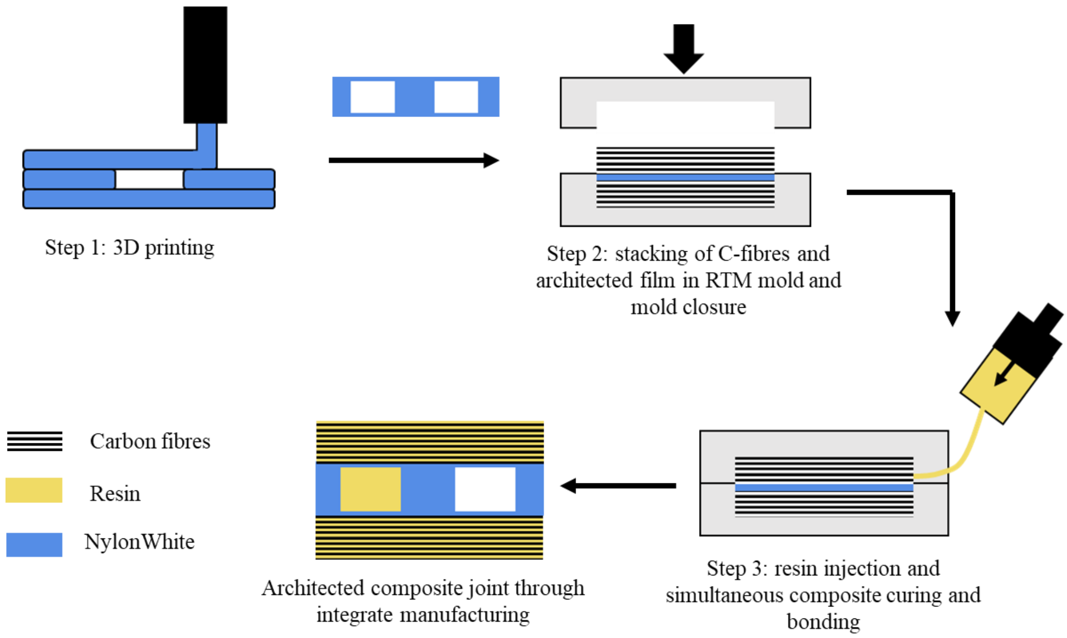

Figure 2: Manufacturing steps for architected joints from 3D printing of the architected Nylon part to the unmolding.

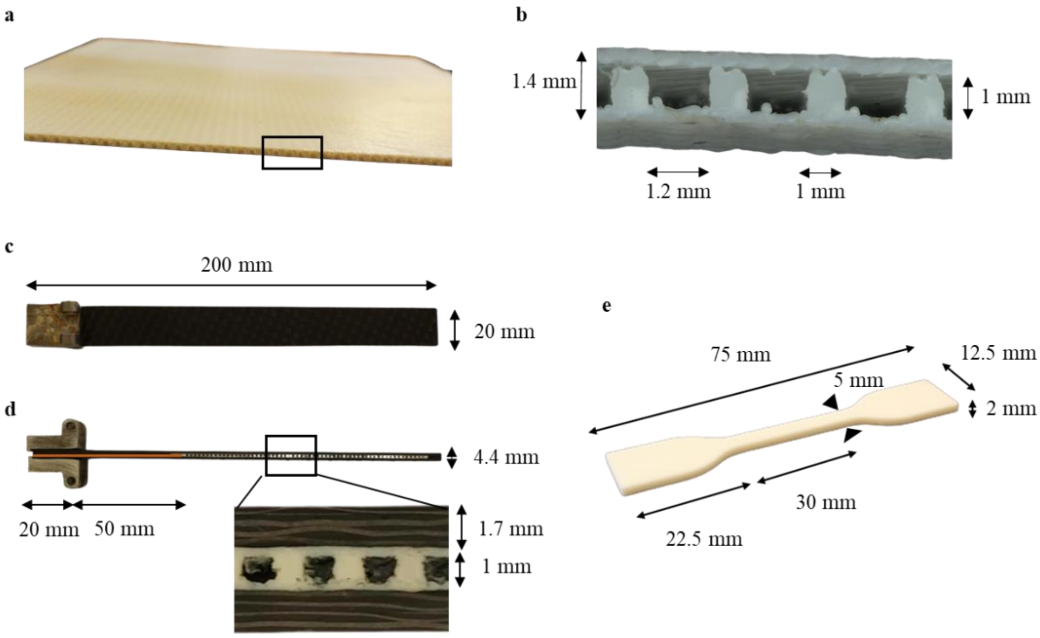

Figure 3: Nylon film and specimens with their dimensions: (a) Nylon film after 3D printing, (b) zoom on the edge of the Nylon film with the dimensions of the cavities after printing, (c) DCB specimen from the top, (d) lateral view of the DCB specimen and zoom on the film after bonding, (e) tensile specimen.

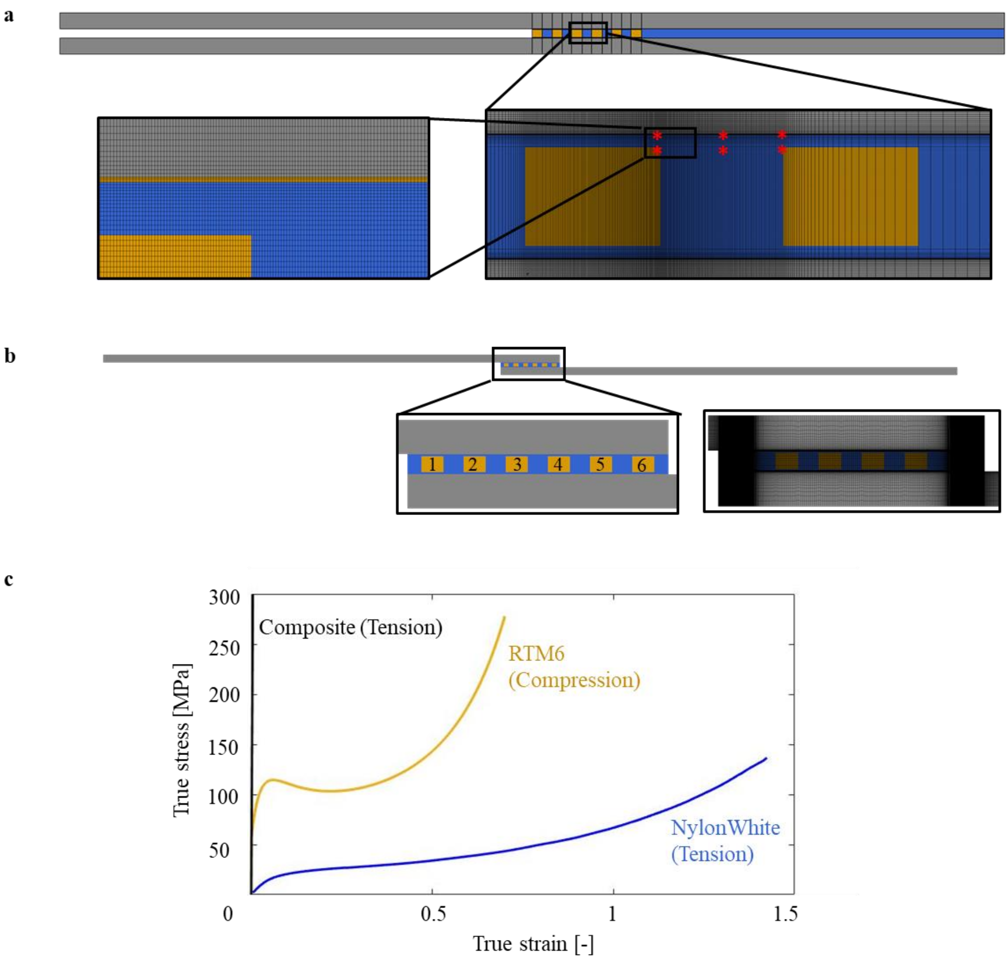

d

	E [MPa]	σ_y [MPa]	σ_f [MPa]	ε_f [-]	σ_c [MPa]	l_c [µm]
Composite	70 000	/	860	0.012	NA	NA
NylonWhite	400	23	136	1.42	50	200
RTM6	3 000	114	275	0.7	300	10
RTM6 interface	3 000	114	275	0.7	50	100

Composite Nylon Epoxy resin * Potential crack tip positions

Figure 4: Geometries of the finite element model and corresponding mesh: (a) Double Cantilever Beam configuration and (b) Lap-shear configuration. (c) Engineering stress-strain curve data for NylonWhite, RTM6 and the composite used to model the Nylon film. (d) Properties of the materials and parameters of the failure criterion.

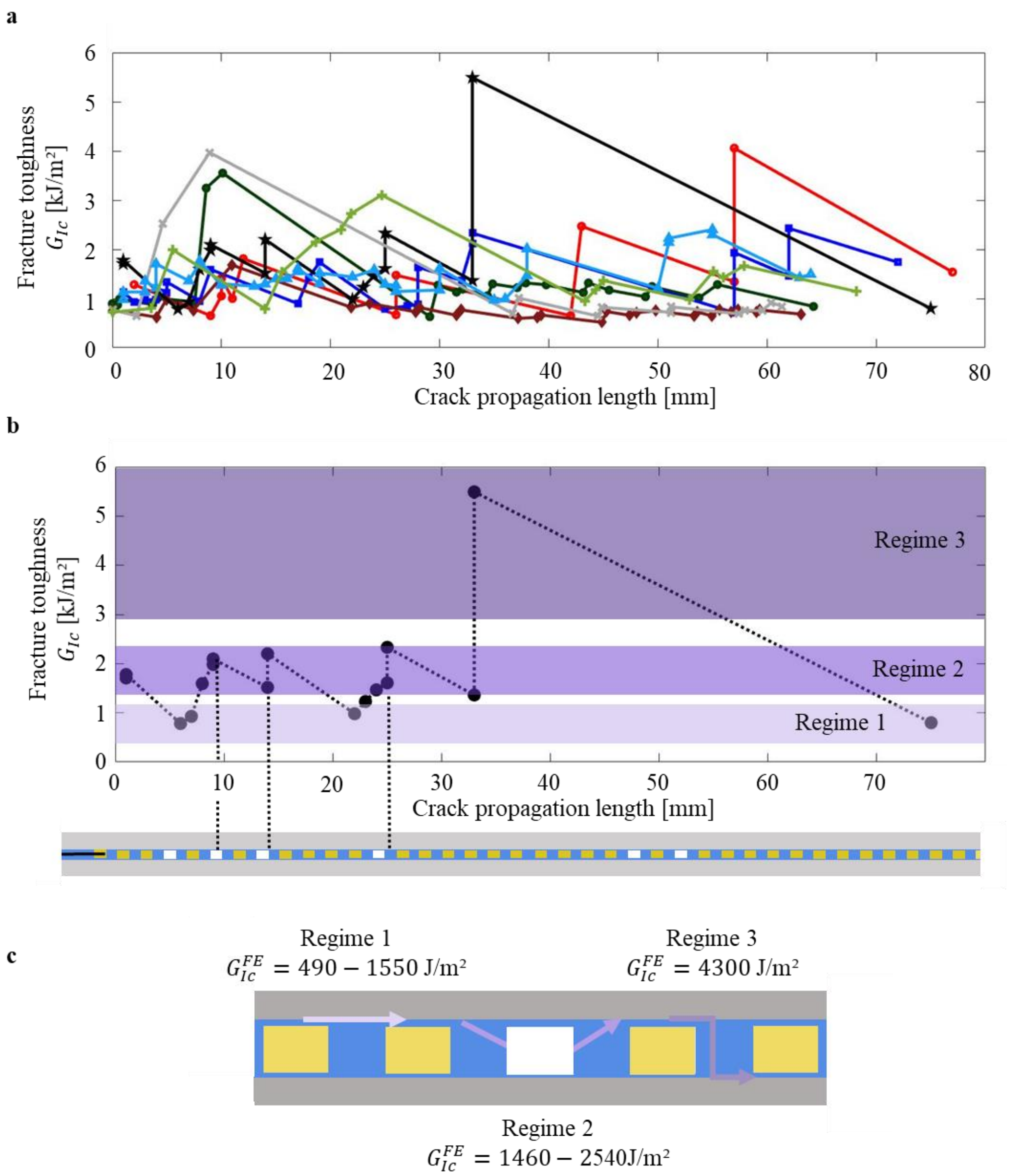

Figure 5: (a) Experimental crack resistance curves for architected joints. (b) One of the R-curves with the associated joint configuration. (c) Microstructure associated to each regime with the G_{Ic} computed by FE modelling.

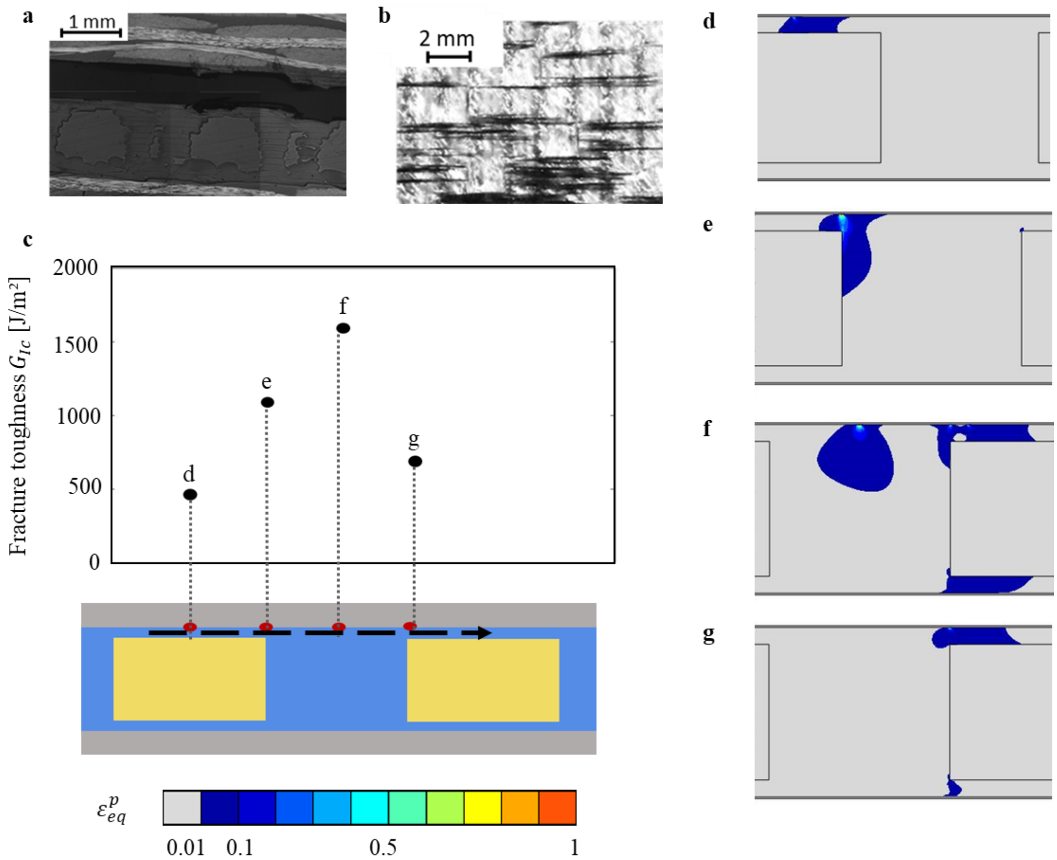

Figure 6: Optical micrographs corresponding to the fracture surface in Regime (1) from (a) the side and (b) the top of the Nylon film. (c) Variation of G_{Ic}*, throught FE modelling, with the crack tip position and the corresponding plastic zones: crack located (d) above the filled cavity, in the middle of it; (e) above the last corner of the filled cavity; (f) between two consecutive filled cavities and (g) above the first corner of the filled cavity.*

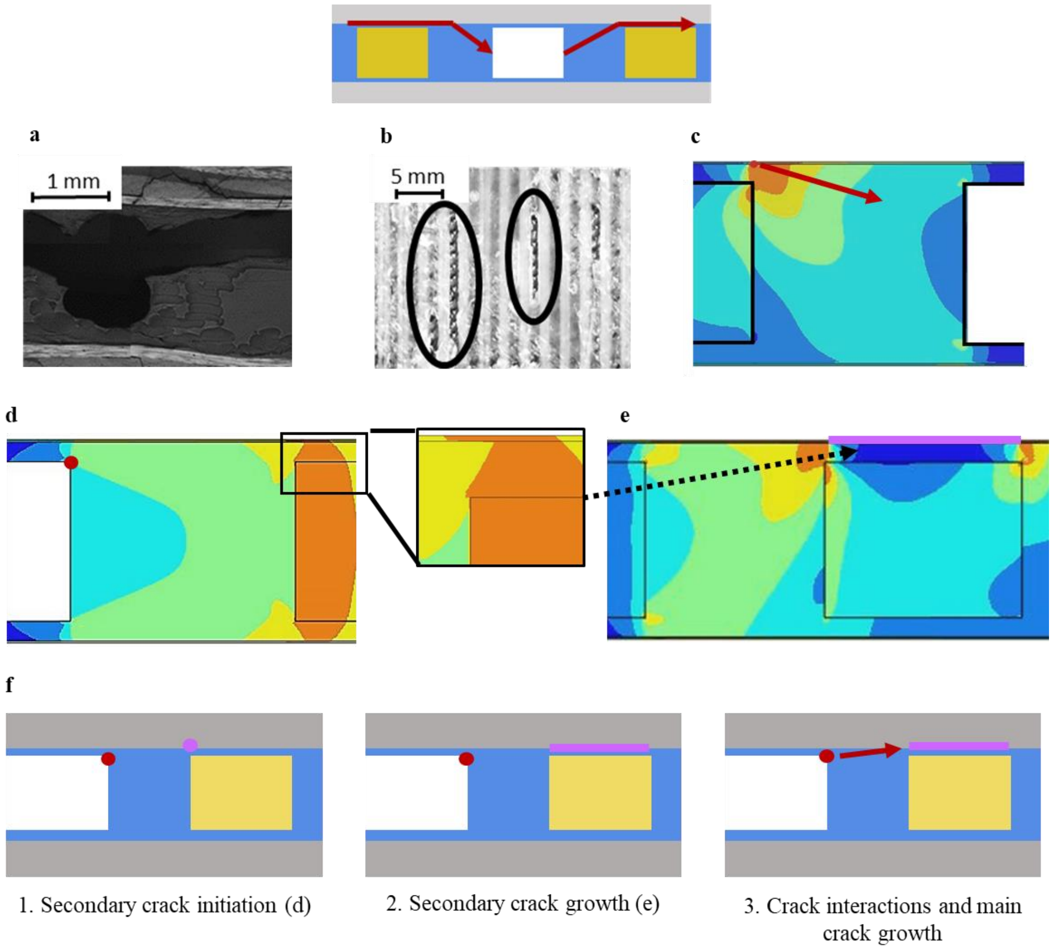

Figure 7: Failure mechanism associated to the presence of an empty channel (Regime 2): (a)-(b) Optical micrographs from (a) the side of the DCB and (b) the top surface of the PA film. (c)-(e) Stress distributions when (c) the crack is located behind the cavity and (d)-(e) the crack is trapped by the cavity (d) before and (e) after secondary crack initiation. (f) Summary of the failure mechanism when the crack has been trapped by the cavity.

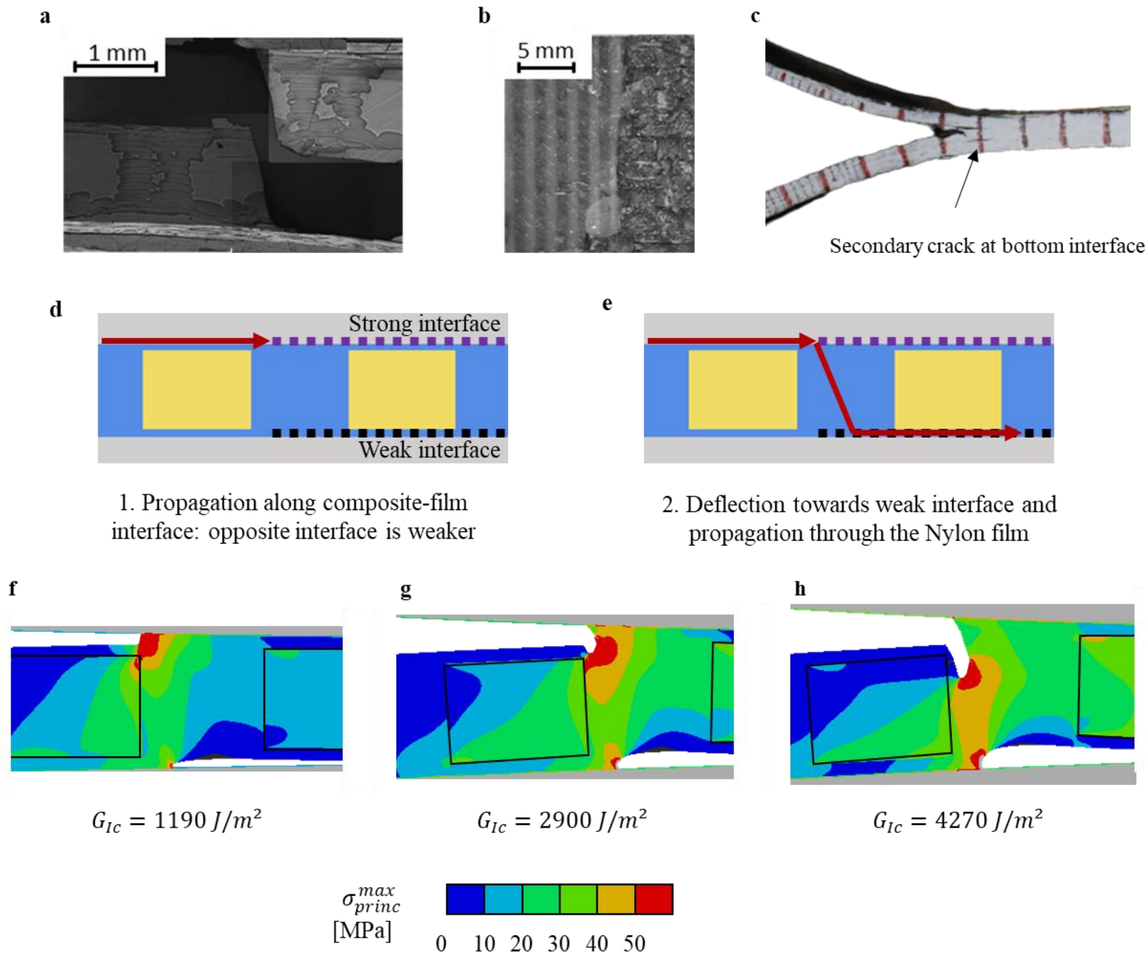

Figure 8 : *Optical micrographs corresponding to the fracture surface in Regime (2) from (a) the side and (b) the top of the Nylon film. Stress distributions when the crack is located (c) before the void, (d) is trapped by the void and (e) when the two cracks interact with each other. (f)-(g) Progressive propagation through the film thickness due to main crack interactions with a secondary crack at the opposite interface.*

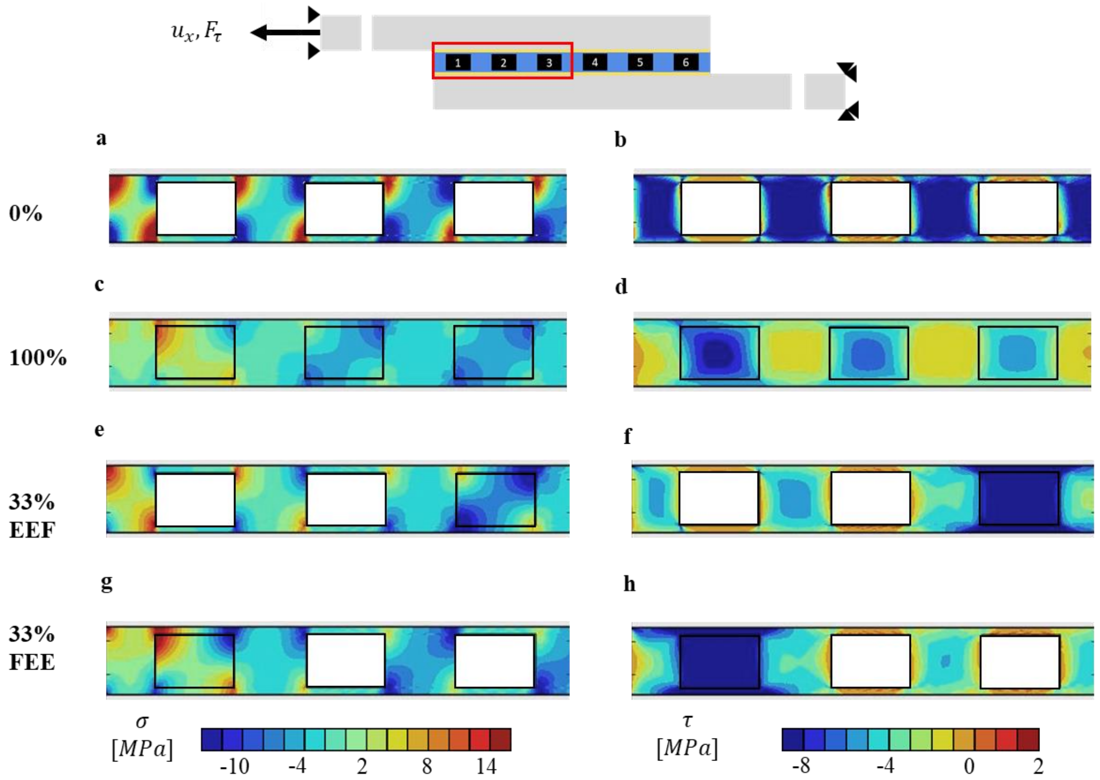

Figure 9: Peel (left) and shear (right) stress distributions in lap-shear joints containing (a)-(b) 0%, (c)-(d) 100%, (e)-(h) 33% of filled channels. (e)-(f) The filled channel is located at the joint center or (g)-(h) at the edge of the lap joint.

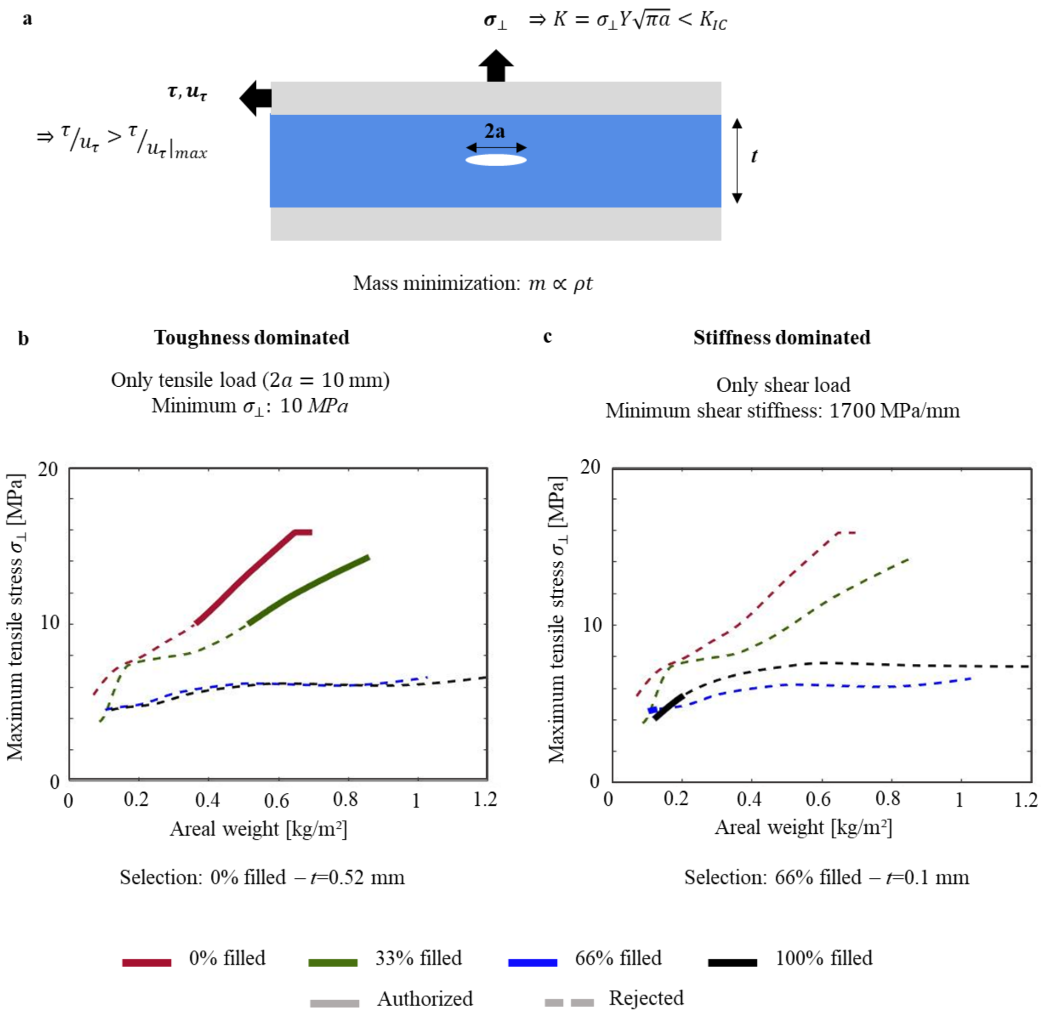

Figure 10: Materials selection approach for architected adhesive joints (a) problem description, (b) case where the toughness dominates the problem due to high peel stress and (c) the problem is stiffness-dominated.

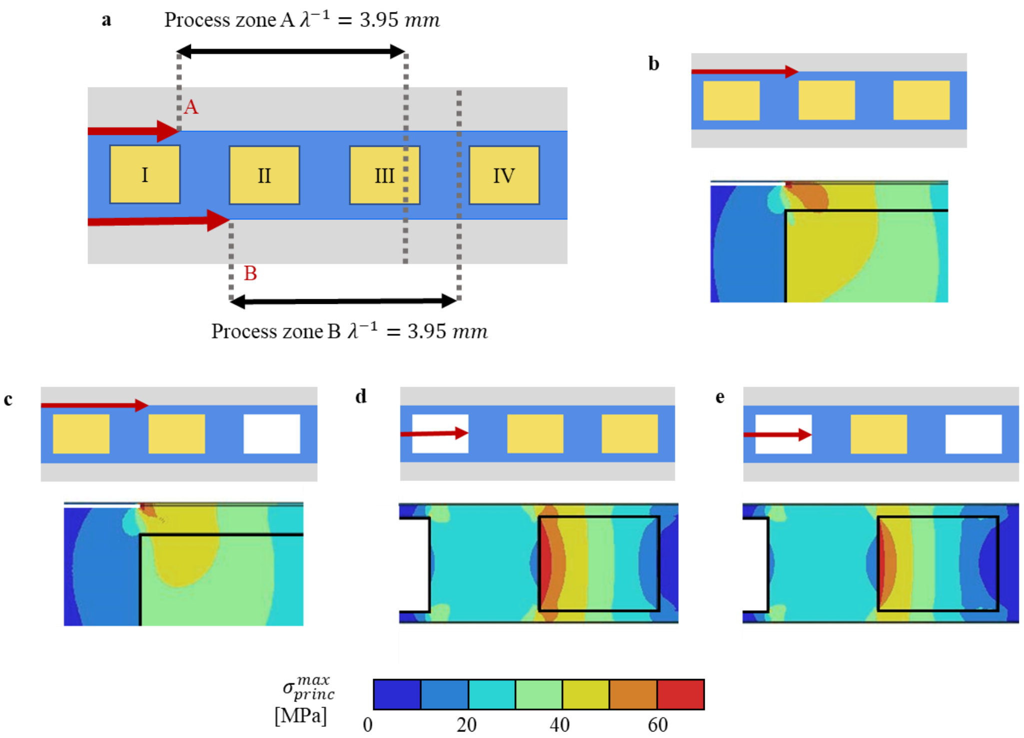

Figure A.1: (a) *Schematic view of the process zone length and the part of the joint covered by this zone if the crack is located at the left (crack B) or at the right corner (crack A) of a channel. (b)-(e) Maximum principal stress distribution when (b) and (c) the crack propagates along the interface and (d)-(e) when the crack has been trapped by a cavity and the first cavity ahead of the crack tip is full of resin. In (b) and (d), the last considered cavity is filled while in (c) and (e) it is left empty resulting in an anti-shielding effect.*

Table 1: Joint stiffness, strength and fracture toughness of architected joints depending on the configuration.

Amount of filled cavity	Configuration	Apparent shear modulus [MPa]	Strength [MPa]	Maximum G_{IC} *[kJ/m²]*
0%	EEE	52	6	40
33%	FEE	138	9	16
	EFE	138	11	16
	EEF	137	12	16
66%	EFF	221	14	2.2
	FFE	222	12	2.2
	FEF	223	13	2.2
100%	FFF	306	14	1.5
Nylon	/	143	12	8.5 – 11.5 [48]
Resin	/	1070	20	0.09[4]